Available online at www.sciencedirect.com
SCIENCE DIRECT®
Journal of Magnetic Resonance 167 (2004) 1–11
JMR Journal of Magnetic Resonance
www.elsevier.com/locate/jmr

Investigating ^{3}He diffusion NMR in the lungs using finite difference simulations and in vivo PGSE experiments

Stanislao Fichele,* Martyn N.J. Paley, Neil Woodhouse, Paul D. Griffiths, Edwin J.R. van Beek, and Jim M. Wild

Academic Unit of Radiology, The University of Sheffield, Royal Hallamshire Hospital, Glossop Road, Sheffield, S10 2JF, England, UK

Received 23 June 2003; revised 23 September 2003

Abstract

Finite difference simulations have been used to model ^{3}He gas diffusion in simulated lung tissue. The technique has the advantage that a wide range of structural models and diffusion-sensitizing gradient waveforms can be investigated, for which analytical methods would otherwise be virtually impossible. Results from simulations and in vivo pulsed-gradient-spin-echo (PGSE) experiments show that the apparent diffusion coefficient (ADC) is a function of diffusion time and gradient strength, and suggests diffusion is locally anisotropic. The simulations have been compared to recent work on an analytical model that characterizes lung tissue as a series of independent cylinders. The results presented may have clinical implications for ^{3}He ADC measurements in assessing lung diseases such as chronic-obstructive-pulmonary-disease.

Keywords: Hyperpolarized; ^{3}He; Diffusion; Finite difference; PGSE

1. Introduction

The introduction of hyper-polarized (HP) noble gas magnetic resonance (MR) imaging has shown much promise for both anatomical and functional imaging of the pulmonary air-spaces [1,2]. An exciting aspect of noble gas imaging is the potential to probe the lung microstructure using diffusivity measurements derived from pulsed-gradient-spin-echo (PGSE) techniques [3]. The confining length scales within the lungs are generally small (<0.6 mm) compared to the distance of unrestricted diffusion of a ^{3}He atom during a typical MR experiment. This leads to a spatial confinement in ^{3}He gas diffusion, yielding an apparent diffusion coefficient (ADC) which is significantly lower than that of free-space. In healthy volunteers, measurements suggest the ^{3}He ADC value is between 0.1 and 0.2 $\mathrm{cm^2 s^{-1}}$ [4–7], whereas in unrestricted room air the self diffusion coefficient, D_0, is approximately 0.88 $\mathrm{cm^2\,s^{-1}}$ [8].

It has been demonstrated that the ^{3}He ADC value is dependent on gradient timing characteristics and field strength [9,10]. Recent work by Yablonskiy et al. [11], has addressed this problem by using an analytical model which can provide a more quantitative measure of lung microstructure. They treat lung tissue as a series of randomly oriented, independent cylinders (which we will refer to as the "cylinder" model). The results yield two orthogonal diffusion coefficients which can be used to infer the diameters of the alveolar ducts, for which feasible results have been reported.

The work presented here is motivated by the lack of a comprehensive theory describing gas diffusion within the lungs and the need to understand the variation of ADC against *b*-value. We have used preliminary numerical simulations and conducted in vivo experiments to investigate ^{3}He diffusion in lung models over a wide range of diffusion-sensitizing parameters. The simulation results have been analyzed using the cylinder model. Numerical techniques have the advantage that complicated models can be investigated, which would prove virtually impossible to solve using analytical methods alone [12–14].

* Corresponding author. Fax: +44-114-272-4760.
E-mail address: s.fichele@sheffield.ac.uk (S. Fichele).

1090-7807/$ - see front matter © 2003 Elsevier Inc. All rights reserved.
doi:10.1016/j.jmr.2003.10.019

2. Theory of diffusion in independent cylinders and channels

Lung tissue comprises a tortuous system of alveolar ducts and sacs. The recent work reported by Yablonskiy et al., recognizes diffusion in lung tissue as being locally anisotropic, and models the lung as a series of independent cylinders, scattered randomly in all three dimensions (3D). We use this mathematical framework to analyze the models presented in the methods.

In a cylinder the ADC can be characterized by two diffusion components; one directed along the longitudinal direction, D_L, and the other along the transverse direction, D_T. The resulting attenuation of the spin-echo in an infinitely long cylinder can be written as [11,15]

$$S = S_0 \exp(-bD_L \cos^2\alpha - bD_T \sin^2\alpha), \quad (1)$$

where α is the angle between the gradient direction and the principle axis of the cylinder, and b has its usual meaning for a PGSE experiment. The transverse component, D_T, is given by the complicated equations found in [11,16,17], which are functions of gradient timing, gradient strength, and cylinder radius. In the lungs the value of D_L is smaller than that of free-space because the inner walls of the alveolar ducts are not smooth, but are surrounded by alveoli.

In lung tissue there are a large number of alveolar ducts and sacs within each acinus, with their orientation being isotropically distributed. Thus the ADC measurement from one pixel represents an orientational-mean value for all airways. If we consider a series of infinitely long cylinders that are independent, but scattered randomly in many orientations, then the resulting spin-echo attenuation is given by the following summation [11]:

$$S = S_0 \int_0^\pi \frac{F(\alpha)\exp[-b(D_L\cos^2\alpha + D_T(t)\sin^2\alpha)]\,d\alpha}{\int_0^\pi F(\alpha)\,d\alpha}, \quad (2)$$

If the cylinders are scattered isotropically (in all three-directions) then the factor $F(\alpha) = \sin(\alpha)$ [11]. If, however, the cylinders are confined to the xy plane and the gradient direction is also confined to the xy plane (2D) then the factor $F(\alpha) = 1$. The latter situation is also applicable to independent 2D channels/branches dispersed uniformly within a 2D plane. However, in the 2D case D_T should be calculated using the solution for diffusion within a planar boundary, e.g., Eq. (15) from [16].

As expected the results reported in [11] yielded values for D_L which were much smaller than D_0 in healthy lungs. The measured values for D_T were used to calculate the average diameter of the alveolar ducts, which gave physiologically plausible results ($\approx$0.7 mm). Despite this, the alveolar ducts are interconnected, and it is hence desirable to determine how well the "cylinder" approximation describes diffusion in both healthy and diseased lung.

3. Methods

3.1. Finite difference method for diffusion

Diffusion in MR can be modeled using finite difference (FD) techniques [18], which can allow great flexibility in assessing complex structures such as the lungs. In order to simplify the calculations we make the following assumptions. (1) Transverse relaxation, T_2^*, can be ignored since the ADC can be measured using sequences that use interleaved strategies with reference image scans conducted at the same echo-time. (2) No convection or bulk flow of magnetization exists, which is reasonable since in vivo experiments are conducted whilst the volunteer holds their breath. (3) Helium is virtually insoluble in blood, and therefore the alveolar walls can be treated as impenetrable. (4) Any background gradients that may arise from B_0 inhomogeneity are ignored. (5) The ADC is calculated from the attenuation of the spin-echo, thus only the transverse component of the magnetization is modeled, and the longitudinal component is ignored. (6) Prior to the application of the bipolar diffusion-sensitizing gradient, the magnitude and phase of the transverse magnetization is uniform, and coherent throughout the simulation volume.

The *Bloch–Torrey* equation can be written as

$$\frac{dM}{dt} = -i\gamma(G_x x + G_y y + G_z z)M + D\nabla^2 M, \quad (3)$$

where M is a complex number. Its real part represents the magnetization along the x-axis of the rotating frame and its imaginary part represents the y-component. G_x, G_y, and G_z are the gradient amplitudes in the x, y, and z directions. D is the diffusion coefficient.

This equation can be solved numerically by breaking it into two iterative parts. The gradient part of Eq. (3) acts as a rotation term, which is responsible for incrementing the phase of the magnetization. In the absence of diffusion we can solve this by a *Taylor* expansion, thus obtaining the difference solution for the magnetization at a time $t + \Delta t$ later

$$M(t+\Delta t, x, y, z) = M(t, x, y, z)\exp(-i\gamma(G_x x + G_y y + G_z z)\Delta t). \quad (4)$$

The diffusion part of Eq. (3) can be solved by finite-difference. There are many possibilities here, however, we adopted the most basic *explicit* scheme, which in one dimension can be implemented in two simple steps [19]

$$M_j' = M_j^n + D_{j-1,j}\frac{\Delta t}{\Delta x^2}(M_{j-1}^n - M_j^n), \quad (5)$$

$$M_j^{n+1} = M_j' + D_{j,j+1}\frac{\Delta t}{\Delta x^2}(M_{j+1}^n - M_j^n), \tag{6}$$

where M_j^n is the magnetization at jth position along the x-axis and at the nth time step, hence $M_j^n \equiv M(x,t)$, with $t = n\Delta t$ and $x = j\Delta x$. M_j' is an intermediate quantity. $D_{j,j+1}$ represents the effective diffusion coefficient between the jth and $(j+1)$th element. These equations represent a discrete version of Fick's first law of diffusion, with Eq. (5) equating to diffusive exchange with the left element and Eq. (6) being the contribution from the right hand element. An impermeable barrier can be created between two elements by setting either $D_{j-1,j}$ or $D_{j,j+1}$ to zero in either equation, see Fig. 1. This scheme can be converted to three dimensions in a variety of different ways. The easiest is to apply the above procedure (Eqs. (4)–(6)) at each time step first along the x-direction, then along the y-direction, and finally along the z-direction.

In-house code was developed in *Matlab* (Mathworks, Natick) and *C*. Calculations were performed on a *Dell Precision* workstation (Austin, TX) equipped with 1 giga byte of random-access-memory, and a 1.6 GHz central processing unit. Data were stored using IEEE double precision to allow sufficient precision for the calculations. The diffusion algorithm was then run using the iterative steps of Eqs. (5) and (6). However, if an element was tagged as being tissue then it was ignored or the corresponding $D_{j,j+1}$ coefficient was set to zero. Similarly, the elements tagged as "tissue" were also ignored in the phase increment step Eq. (4).

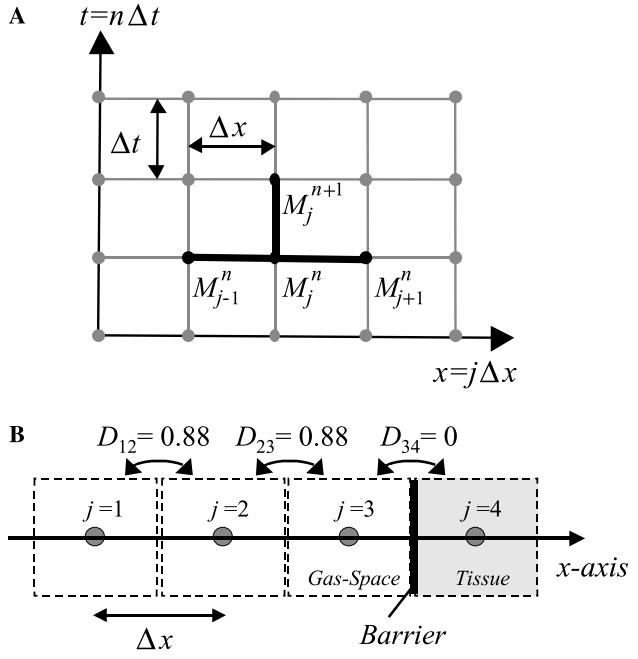

Fig. 1. (A) Finite difference scheme in 1D. The magnetization is represented by a series of points, evenly spaced along the x-axis. The magnetization at the next time step $(n+1)$ is calculated explicitly by using the magnetization at the nth time step. Only the magnetization at elements $j-1$, j, and $j+1$ are required to calculate M_j^{n+1}. (B) Diffusion between elements; where two gas-space elements reside adjacent to one another, the inter-element diffusion coefficients are set to D_0 that of self diffusion in free-space. A barrier between a gas-space element and a tissue element can be created by setting the inter-element diffusion coefficient to zero.

To simplify the simulations further, the bipolar gradient waveform had no delay between the negative and positive lobes, and the rise-time was set to zero. At the end of a simulation the ADC value was calculated by summing the complex magnetization, and then taking the modulus value. The ADC was then calculated using the following summation:

$$\mathrm{ADC} = \frac{1}{b}\log\left\{\sum_{i=1}^{N} F(\alpha_i)\right\} - \frac{1}{b} \times \log\left\{\sum_{i=1}^{N} F(\alpha_i)S(\alpha_i, b)\right\}, \tag{7}$$

where $S(\alpha_i, b)$ is the normalized magnetization that is obtained for each gradient orientation α_i, and is equivalent to

$$S(\alpha_i, b) \equiv \exp\left[-b\left(D_{\mathrm{L}}cos^2\alpha_i + D_{\mathrm{T}}\sin^2\alpha_i\right)\right]. \tag{8}$$

Elements pertaining to tissue were discounted during the calculation of the ADC.

3.2. Boundary wrapping

In order to keep computation times to a minimum the size of the arrays must be kept small. However, this leads to edge effect problems since gas can not penetrate the peripheral boundaries of the simulation volume. To overcome this problem we implemented a simple boundary wrapping technique where magnetization could diffuse from one boundary to its opposite boundary. The technique was equivalent to repeating the simulation volume infinitely in all directions. Take for example diffusion along the x-axis at element $j = 1$. With boundary wrapping, Eq. (5) was applied to find the diffusive exchange between elements $j = 1$ and $j - 1 = N_x$, where N_x is the number of elements along the x-axis. However, there is a phase discontinuity between these elements which is due to the application of the gradient. Thus a phase subtraction of

$$\varphi_x(t) = \Delta x N_x \int_0^t \gamma G_x(t')\,\mathrm{d}t', \tag{9}$$

must be made to the phase of element $j - 1 = N_x$ prior to applying Eq. (5). Whereas to evaluate the magnetization at element $j = N_x$, using Eq. (6), the phase of element $j + 1 = 1$ must be increased by the amount in Eq. (9). Similar phase corrections were applied for all directions in which boundary wrapping was desired.

3.3. Stability, convergence, and choice of parameters

In order to stop the simulations from diverging, the choice of parameters, Δx, Δt, G_x, G_y, G_z, and δ were carefully selected. For stability the following relation must hold [19]:

$$k \equiv D\frac{\Delta t}{\Delta x^2} < 0.5. \tag{10}$$

Empirical tests for 3D simulations revealed that k should be set to less than 0.3, and that accuracy could be increased by decreasing the value of k (at the expense of computation time). For 3D simulations using conservative array sizes (e.g., $100 \times 100 \times 100$), simulation times can be of the order of days. Thus in all simulations a (maximum) value of $k = 0.27$ was chosen since it satisfied the stability criteria, but minimized the total computation time.

There is also a limit on the physical spacing, Δx, between elements, since the application of the gradient causes the real and imaginary parts of M to vary sinusoidally. Hence, in order to satisfy the Nyquist criteria the size of Δx must be smaller than

$$\Delta x < \frac{\pi}{\gamma G_x \delta}. \tag{11}$$

It was found empirically that a more stringent criteria than Eq. (11) was required. In virtually all cases Δx should be at least 10 times smaller than the Nyquist size if the simulation accuracy was to exceed 1%.

3.4. Overview of models

The ADC can be interpreted as measuring gas diffusion within the acini of the lungs, where respiration takes place, and constitutes approximately 95% of the total lung gas volume [20]. Therefore to simplify the models, only the acinar structure was considered. Each acinus has an approximate volume of $0.15\,\mathrm{cm}^3$, and consists of a complex series of airways that branch-off dichotomously for approximately nine generations [20,21]. The branches which lead to further respiratory channels are termed alveolar ducts, whilst terminal branches are termed alveolar sacs. The inner surfaces of each airway are comprised from the mouths of mural alveoli which are typically 0.25 mm in diameter, yielding airways that are approximately 0.7 mm in total diameter (alveoli included). There are an average of 20 surface alveoli per alveolar duct, and each duct is typically between 0.5 and 1.5 mm in length [21].

In the work presented here, three simple structural types were investigated which were deemed appropriate to emulate lung tissue: a heterogeneous porous structure, a "grape-vine" model, and a "tree-like" model. These are depicted in Fig. 2.

It has been speculated that porous models may be suited to describing lung tissue. Recently, PGSE diffusion measurements have been made in packed bead phantoms and sedimentary rocks using xenon gas [22,23]. The experimental results can potentially be used to determine the surface-area to volume ratio of the pores [24], thus such measurements could prove beneficial in analyzing lung tissue. We investigate diffusion in porous structures with length scales that are representative of lung tissue, and use pulse sequence parameters which are typical of in vivo ADC measurements.

The tree- and grape-like models consist of dichotomously dividing branches that comprise the main structure which confines the gas. In the "grape-like" model the branches open up to additional compartments, as do the alveoli in the lung. We can analyze the results from these structures using the mathematical framework of [11] as an approximation.

3.5. The porous model

A large range of porous structures were assessed with a range of b-values which were deemed suitable for MR imaging ($\delta = 0.2 \rightarrow 4.0\,\mathrm{ms}$, and $G = 8 \rightarrow 24\,\mathrm{mT\,m^{-1}}$). The porous models were generated by stacking pore shapes in a hexagonal-closed-packed lattice formation [25]. 3D pores were constructed from the locus of the following function:

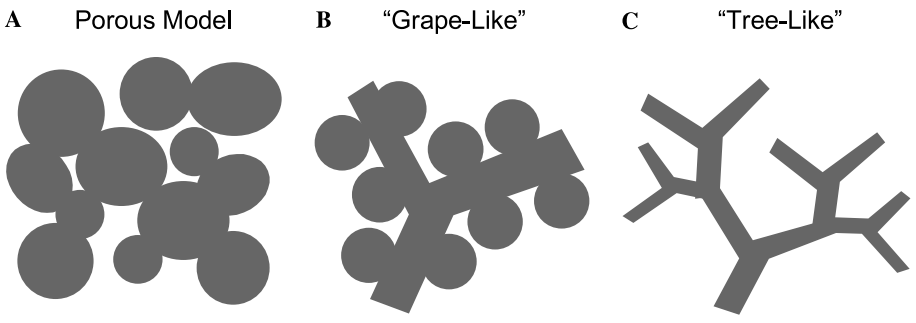

Fig. 2. Models of lung tissue, the gray areas represent gas space. (A) A porous model, consisting of interconnected pores of different shapes and sizes. (B) A "grape" model, consisting of a branching pattern, with mural alveoli. (C) A plain "tree" like model.

$$\left|\frac{x}{p}\right|^{\theta} + \left|\frac{y}{q}\right|^{\phi} + \left|\frac{z}{r}\right|^{\varphi} \leqslant 1, \quad (12)$$

where $2p$, $2q$, and $2r$ are the effective diameters of the pores along the x, y, and z directions. The values of the exponents θ, ϕ, and φ were varied randomly to control the amount of curvature of the pores, which ranged between 2.0 and 3.0.

A total of 12 structures were generated with pore sizes that ranged between 78 and 630 μm in diameter. The openings between the pores could be controlled by varying the mean lattice spacing, which was typically set between 0.9 and 1.4 times the average pore size. Also, the position of the pores were allowed to deviate randomly from the HCP lattice by approximately 0–40% of the average pore size, which introduced further heterogeneity in the structure.

In order to obtain structures with sufficient resolution the element sizes, Δx, typically ranged between 5 and 15 μm. The simulations took between one and 10 days to yield spin-echo attenuations for five or more b-values. These large computation times limited the study to just one gradient direction, which was along the x-axis.

3.6. The tree-like and grape-like models

Ideally the tree-like and grape-like models would be generated in 3D using a parameter driven system that used physiologically accurate dimensions. However, such a computational model would be difficult to realize. Instead we opted to generate the models in 2D using hand-drawn elements created with an art package (*PowerPoint*, *Microsoft Corporation*).

The main criteria that influenced design were branch lengths and diameter. Typically the lengths were set to approximately 1 mm, with diameters/widths ranging between ultra-thin (≈45 μm) and 0.32 mm. For the ultra-thin case, branches were only a few elements wide, and thus transverse diffusion could be ignored to investigate the role of branching inter-connectivity on the longitudinal diffusion, D_L. An attempt was made to generate branching angles that were akin to lung tissue. Thus the majority of branches were adjoined to parent branches with angles smaller than 30°. Tissue destruction, in diseases like emphysema, was emulated by creating additional pathways between otherwise independent branches, and greatly widening and distorting the shapes of the underlying branches. Also some branches were merged together to create larger airways.

The lack of a 3D generation method meant diffusion simulations had to be performed in 2D. In order to facilitate a basic comparison between the 2D simulations, the in vivo results, and the "cylinder" model, the mean ADC for each simulation was calculated using Eqs. (7) and (8), with $F(\alpha_i) = \sin \alpha_i$.

This can be viewed as an extension of the simulation data from 2D to 3D, but represents an approximation to the problem. In part this was deemed acceptable since the part of the aim was to investigate how well the simulation would resemble diffusion in independent channels/cylinders. Thus as a means of facilitating a comparison with the Yablonskiy model the approximation was thought justifiable.

3.7. In vivo methods

The dependence of ADC upon b-value was investigated on volunteers using a variety of pulse gradient waveforms. All studies were performed with local ethical approval. Hyperpolarized ^{3}He was produced on-site using a commercial polarizer (*Amersham Health, Durham NC*). A total of 1.2 L of ^{3}He, polarized to approximately 30%, could be generated over a period of 20 h. The ^{3}He gas was then decanted into plastic Tedlar bags (*Jensen Inert, Florida*) and diluted with pure nitrogen (600 ml 3He and 400 ml N_2). All in vivo imaging experiments were conducted at 1.5 T using a whole-body MR scanner (*Eclipse, Philips Medical Systems, Cleveland Ohio*) which was equipped with a gradient set that could deliver a maximum gradient pulse of 27 mT m^{-1} in a minimum rise time of 375 μs. ^{3}He images were acquired using a quadrature radio-frequency transmit/receiver coil with a flexible twin saddle design (*Medical Advances*, *IGC*, *Milwaukee*, *Wisc.*), tuned to the ^{3}He Larmor frequency of 48.5 MHz.

Two dimensional ^{3}He images were encoded using a standard gradient echo sequence, employing a small flip-angle of approximately 6^0. Diffusion-sensitizing gradient pulses were added perpendicularly to the image plane using the pulsed gradient method of Stejskal and Tanner [3]. For each slice a total of six separate images were acquired in an interleaved fashion with different diffusion weighting. That is the same line of k-space was sampled six times, using different b-values, before stepping to the next one. Interleaving in this fashion ensured a reduced sensitivity to motion artifacts [5] and allowed easy correction of flip-angle loss.

Two volunteers underwent breath-held imaging experiments in the supine position. The first volunteer was a healthy male, aged 33. The second was a female (healthy) smoker, aged 51, who was chosen from a previous study since her ADC maps demonstrated a wide range of ADC values. The main imaging parameters were: five 20 mm thick axial slices, 10 mm slice gap, 40 cm field-of-view (FOV), 48 phase encode steps, 128 data samples (over-sampled to 256), 20 μs sampling time. Images were acquired with echo-times (TE) ranging between 8.5 and 11.5 ms, and repetition-times (TR) ranging between 11 and 14 ms. Note that for a particular imaging experiment TE and TR remained fixed for all interleaves. In each imaging experiment, the first and the last interleaved images had no diffusion weighting, and

were used to determine the overall flip-angle. The data was corrected for flip-angle prior to calculating the ADC. The remaining four interleaves were encoded using b-values of 1.438, 2.695, 4.377, and 6.932 $cm^2\,s^{-1}$. A variety of gradient strengths and pulse durations were chosen to achieve these b-values, which are shown in Fig. 3. In the case of the healthy male, four sets of diffusion schemes were acquired, whereas only two diffusion schemes were acquired for the female smoker.

4. In vivo results

The results for both volunteers are summarized in Fig. 3. For each imaging experiment the maximum pixel intensity in the first interleaved image was typically 100 times larger than the standard deviation of noise. A total of 10 regions-of-interest were assessed (two per slice). The mean ADC values, corresponding to the 2nd, 3rd, 4th, and 5th image interleaves, were calculated using

$$\mathrm{ADC}(i) = \frac{\log S(1) - \log S(i)}{b(i)}, \tag{13}$$

where i denotes the ith image interleave, and $S(1)$ is the MR signal from the first interleaved image. In all cases the ADC value was a strong function of b-value and gradient strength, and in general the ADC value decreased significantly with increasing diffusion time, increasing gradient strength, and increasing b-value. The "cylinder" model was used to determine the mean radii of the alveolar ducts and sacs. In each case this revealed plausible values which were in agreement with the previous results reported by Yablonskiy et al. [11]. For the healthy male, the mean radii of the airways was measured to be between 0.32 and 0.36 mm, and the ADC values were within the typical range expected. A small variation of ADC was seen between each region-of-interest, which is attributed to a systematic variation of alveolar density and size in the superior–inferior direction [7,11,26]. For the female smoker, the measured radii ranged between 0.32 and 0.40 mm. However, in the regions demonstrating very high ADC values the data deviated quite significantly from the "cylinder" theory, and a best fit to the data was not possible.

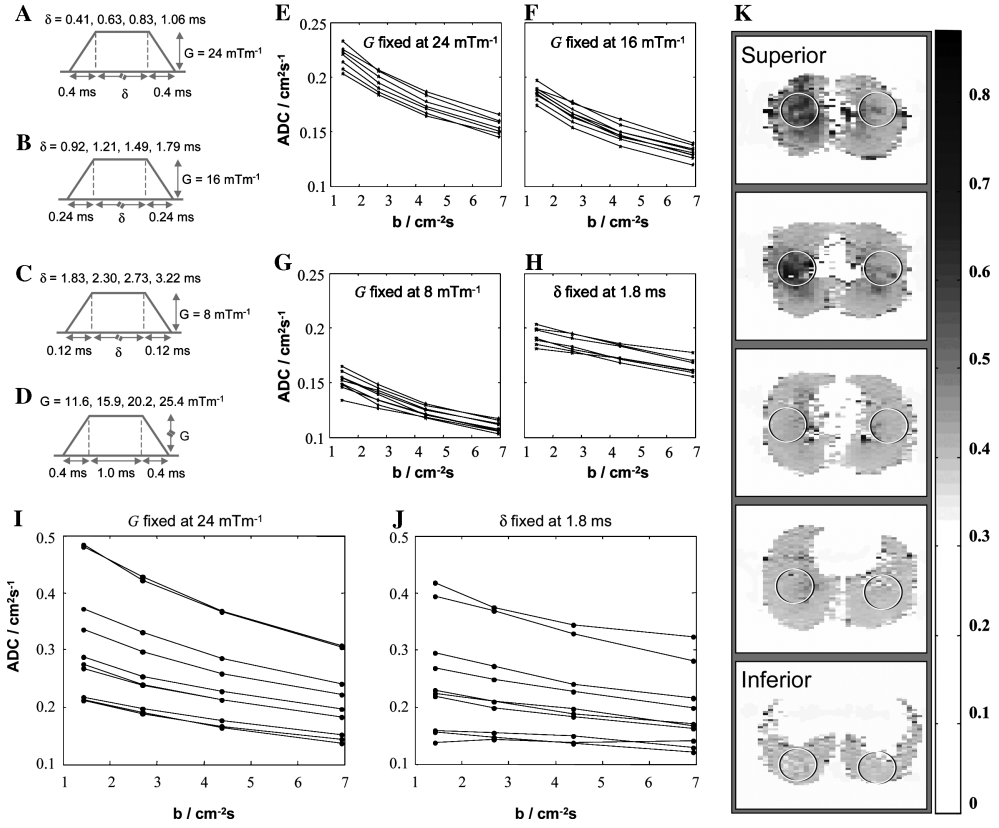

Fig. 3. Five axial ADC maps of different slices of a healthy male (aged 34) and a female smoker (aged 51) were acquired using a range of different b-values and gradient duration. The parameters used for each diffusion sensitizing scheme are shown in (A) through to (D). The curves plotted in graphs (E) through (H) correspond to the mean ADC from 10 regions-of-interest (ROI) taken from the healthy male. The data in graphs (I) and (J) were taken from the female smoker. The axial ADC maps for the female smoker and the corresponding ROIs are presented in (K) for a b-value of 1.43 $cm^2\,s^{-1}$. See text for a discussion of the results.

5. Simulation results

5.1. Validation of boundary wrapping

In order to validate the simulation methods a range of simple tests were performed. The most pertinent was conducted on an infinitely long two dimensional channel. The 2D channel was modeled using an array of 28×10 elements in the x- and y-directions. Boundary wrapping was used in the y-direction to create an infinitely long channel, but was not employed in the x-direction in order to confine diffusion to a planar boundary. The element size was 10 μm, yielding a channel width of 280 μm. Attenuation curves were calculated for a total of 30 gradient orientations $(0, \frac{1}{29}\pi, \ldots, \frac{28}{29}\pi, \pi)$, using a range of b-values with different gradient strengths and durations. The results were then summed using Eq. (7), with $F(\alpha_i) = 1$, to yield an orientational mean ADC, these are summarized in Fig. 4. The longitudinal diffusion coefficient, D_L, was set to that of ^{3}He in room air ($0.88\,\mathrm{cm^2\,s^{-1}}$), and the transverse component, D_T, was calculated from Eq. (15) given in [16]. The simulation results agree well with the simple theory provided and serve as a validation for the boundary wrapping technique.

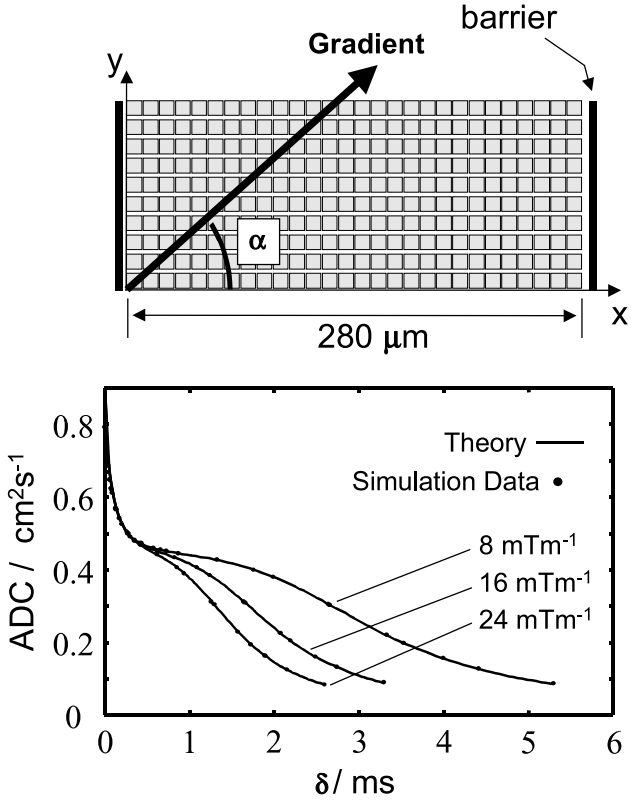

Fig. 4. Simulations were performed on an infinitely long 2D channel, with a width of 280 μm. Attenuation curves were calculated for 10 gradient orientations $(0, \frac{1}{9}\pi, \ldots, \frac{8}{9}\pi, \pi)$ and then summed to find a mean ADC value. Different b-values were achieved by varying the duration of the gradient pulse. Attenuation curves were calculated for three gradient strengths, 8, 16, and $24\,\mathrm{mT\,m^{-1}}$. The size of the 2D array was 28×10 elements in the x- and y-directions. Boundary wrapping was used in the y-direction to make the channel seem infinitely long. The simulation results agree extremely well with theory (see text) and serve as validation for the boundary wrapping technique.

5.2. Porous media

Simulations were performed on 3D porous structures as described in Section 3. It was clear from the results (which are not shown here) that the effect of impermeable peripheral boundaries dominated the ADC curves when the total length of the simulation volume in the x-direction was "short" compared to the average diffusion length $\sqrt{2\delta D_0}$. In fact the results were found to match exactly with restricted diffusion within a planar box [16]. Thus only results from simulation volumes that utilized the boundary wrapping method or had a sufficiently long length in the x-direction were considered.

A typical result that sufficiently summarizes all our results is shown in Fig. 5. As expected the ADC was lower than D_0, however, it was found to be virtually independent of b-value for the range of diffusion parameters studied. All of the simulations we conducted, for all porous structures yielded a similar trend of results for the gradient waveforms studied. The asymptotic values in ADC ranged between 0.1 and $0.8\,\mathrm{cm^2\,s^{-1}}$, however, no correlation was found that linked pore size, and the size of pore openings to the ADC value. The results suggest that these kind of porous structures do not emulate gas diffusion in healthy lung tissue since the ADC is independent of b-value.

5.3. Tree-like results

The results for the "tree-like" formations are summarized in Fig. 6. In each simulation a total of 30 gradient orientations $(0, \frac{1}{29}\pi, \ldots, \frac{28}{29}\pi, \pi)$ were investigated, each using 12 different b-values that were obtained by changing the gradient strength $(2, 4, \ldots, 22, 24\,\mathrm{mT\,m^{-1}})$. The duration of the gradient, δ, was fixed at 1.8 ms. The resulting attenuation curves were summed according to Eq. (7), with $F(\alpha_i) = \sin\alpha_i$, to obtain a mean-orientational ADC. In Fig. 6A the branches were made extremely thin (≈45 μm) so as to neglect any transverse diffusion, i.e., $D_T = 0$. The length of each branch was set to 1 mm. The results are summarized in the table given in Fig. 6E. The longitudinal diffusion coefficient, as derived for the entire structure was found to be $0.6\,\mathrm{cm^2\,s^{-1}}$, however, many of the ADC values computed from magnetization located within individual branches were found to be significantly different, e.g., branch 1, which was found to be $0.46\,\mathrm{cm^2\,s^{-1}}$. Also the ADC from some branches deviated strongly from theory, thus fitting the data yielded unsatisfactory results, e.g., branch 2. We speculate that the variation in ADCs from one branch to

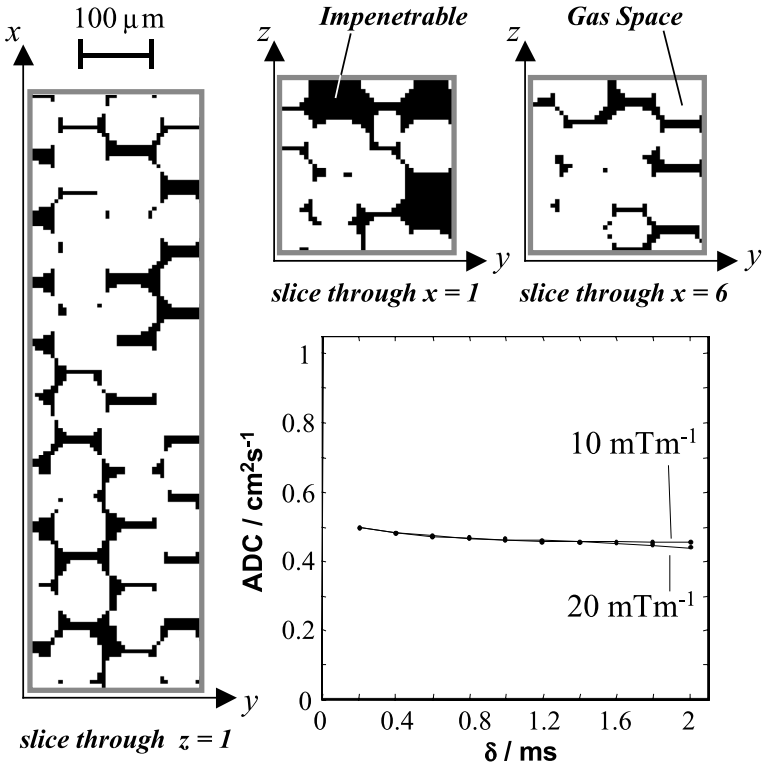

Fig. 5. Here the lung was modeled as a porous structure. The pore diameters varied between 83 and 89 µm. The total array size was $770 \times 39 \times 39$, with an element spacing of 6.5 µm (not all of the simulation volume is shown along the x-direction). ADC values were calculated for two gradient strengths, 10 and 20 mT m^{-1}. Ten different b-values were created by changing the duration of the gradient lobes, δ. Only gradients, directed along the largest length of the simulation volume, were investigated.

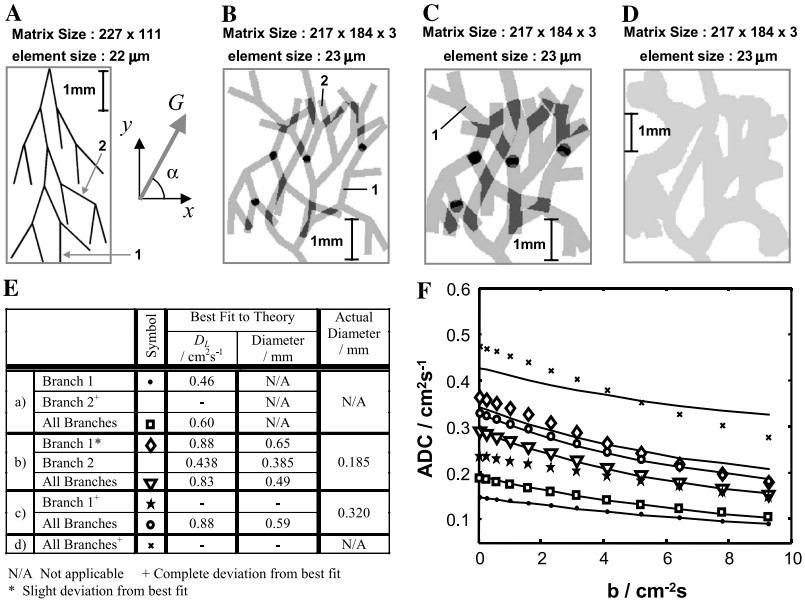

		Symbol	Best Fit to Theory D_{fit} / cm^{2}s^{-1}	Best Fit to Theory Diameter / mm	Actual Diameter / mm
a)	Branch 1	•	0.46	N/A	N/A
	Branch 2+		-	N/A	
	All Branches	□	0.60	N/A	
b)	Branch 1*	◇	0.88	0.65	0.185
	Branch 2		0.438	0.385	
	All Branches	▽	0.83	0.49	
c)	Branch 1+	★	-	-	0.320
	All Branches	○	0.88	0.59	
d)	All Branches+	×	-	-	N/A

N/A Not applicable + Complete deviation from best fit
* Slight deviation from best fit

Fig. 6. Simulations were conducted for "tree-like" structures. Different b-values were generated by changing gradient strength, the duration remained fixed, $\delta = 1.8$ ms. In (A) the branches were made thin so that the transverse diffusion coefficient could be approximated as zero. In (B) the diameter of the branches were set to 0.185 mm (the structure was created over two layers, see text for an explanation). In (C) the branch diameter was 0.320 mm. In (D) the same structure as (B) and (C) was taken as a basis, however, additional openings were introduced and the size of the branches were greatly widened to model emphysema. Some of the simulation results are summarized in the table (E) and the graph (F). The list of symbols included within the table correspond to the data in the graph. Solid lines represent a best fit to theory.

another is a result of the different branching angles. Also, the deviation from the cylinder model for some branches is likely to be a result of the branches being comparable in length to the average diffusion length, $\sqrt{2D\delta}$. Hence, the effective D_L is not a constant with respect to diffusion time.

In Fig. 6B simulations were conducted in a tree structure with 2D branches 0.185 mm in width. In order to include a large number of branches within the simulation area, the structures were created in two separate layers. The dark "pins" connect the two layers together. The main branch of the tree tessellates in the longest direction, which allowed the boundary wrapping method to be employed. For the results shown in the table, the data corresponded to theory quite well. However, in all cases the diameter yielded from fitting the data was greatly overestimated. The reason for this is unknown, however, it is likely to be related to the fact that the branches are not infinitely long, and hence, the components D_L and D_T are not strictly independent parameters. Despite this the trend in ADC data did follow a similar trend to the theoretical data, namely a decreasing ADC with an increasing b-value.

In Fig. 6C, the same structure as in Fig. 6B was investigated with wider branches, 0.32 mm in diameter. The theoretical fits to the results for all the branches yielded a large overestimation for the diameters. Again we found that the ADC for some branches deviated quite strongly from theory, an example is branch 1.

In Fig. 6D, the same basis structure was greatly manipulated to simulate emphysema. The size of the and shape of the branches were significantly increased and distorted. Also additional pathways between branches were added. For clarity only one layer of the simulation volume is shown. The results gave a high ADC value, as expected, and deviated significantly from theory since much of the branch like structure had been deformed.

Overall the simulation results fitted the theoretical trend of the cylinder model, even if the predicted diameters were incorrect. The ADC trend suggests that tree-like structures yield anisotropic diffusion that is well described by two diffusion coefficients. However, the results do not enlighten us to the effects of interconnections and branching angles on the ADC values.

5.4. Grape-like results

Simulations in the "grape-like" structures are summarized in Fig. 7. In each case a total of 16 gradient orientations $(0, \frac{1}{15}\pi, \ldots \frac{14}{15}\pi, \pi)$ were investigated, with gradients of fixed duration ($\delta = 1.8$ ms). Twelve different b-values were obtained by changing the gradient

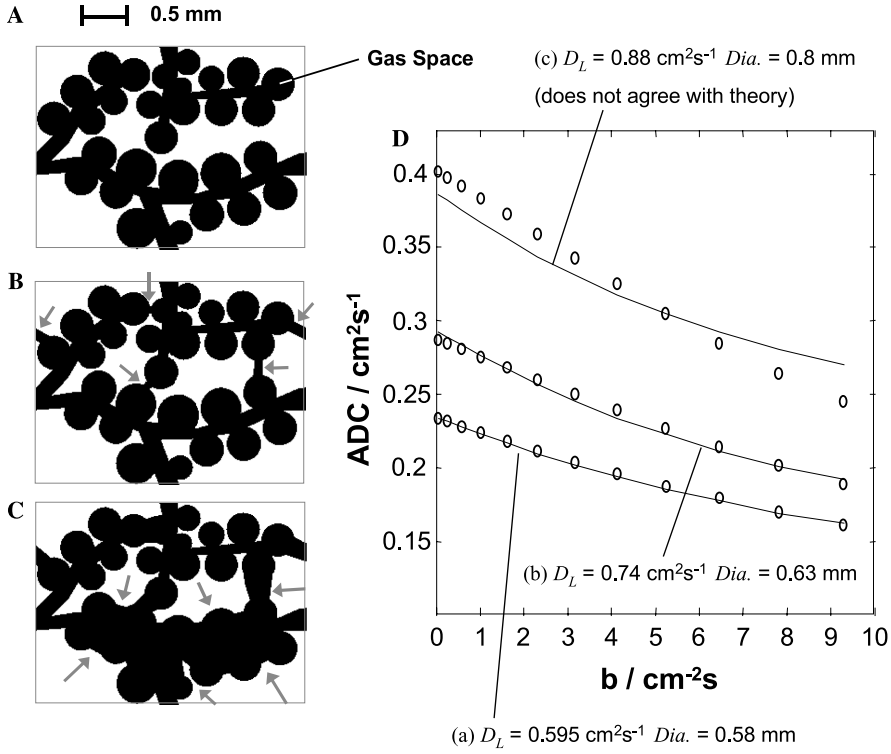

Fig. 7. Simulations were conducted in "grape-like" structures. The 2D structures (A), (B), and (C) comprised 226 × 291 elements, each 10 μm in size. The branches were designed to tessellate in both directions so that the boundary wrapping method could be used. Simulation (B) is nearly equivalent to simulation (A), however, additional pathways between the main branches have been added (highlighted by arrows). In (C) the lowest branch has been greatly widened to emulate emphysema. (D) The data in the graphs correspond to the mean ADC value from the entire simulation area calculated from 30 gradient directions (see text). Solid lines correspond to a best fit to theory, circles are simulation data.

strength (2, 4, ..., 22, 24 mT m^{-1}). The main simulation structure (shown in Fig. 7A) was made to tessellate in order to make optimal use the simulation area and allow boundary wrapping to be employed. The matrix size of the simulation area was 226×291, with an element size of 10 μm. The diameters of the alveoli ranged between 0.25 and 0.45 mm, which is consistent with lung tissue. In Fig. 7B a few selected branches were joined together by additional channels in order to spoil the branching structure and allow additional diffusion pathways (highlighted with arrows). In Fig. 7C additional lung destruction resembling emphysema was emulated by widening the diameter of the lower branches by a factor of approximately 3.

The results are similar to the those from the "tree-like" simulations. However, the estimated diameters obtained from fitting the data, using Eq. (2), yield plausible values. For simulation (a), the estimated diameter is 0.58 mm and the corresponding longitudinal diffusion coefficient is 0.595 cm^2 s^{-1}. In simulation (b) D_L increases significantly as a result of adding the additional connections, which is expected. However, it must be noted that the estimated diameter also increases to 0.63 mm, whereas it should not have, and we find that there was a minor deviation between the data and the fitted curve. It is clear that the results for simulation (c) do not agree with theory, which is expected when compared to in vivo measurements of lung tissue that demonstrate high ADC values.

The fact that the results in Figs. 7A and B agree quite well with the cylinder model and are similar to results from the tree-like model suggest that diffusion in the lungs is mostly characterized by two diffusion coefficients. The presence of the alveoli-like shapes do not significantly perturb the trend of the ADC as compared to the tree-like results, and is partly expected since helium diffusion is very fast and the diffusion time scales, δ, are quite long in these experiments. Also, the presence of the alveoli acts to reduce the overall value of D_L, as compared to the tree-like structures with large branch widths (e.g., Figs. 6B and C).

6. Discussion

^{3}He gas diffusion was investigated using a finite-difference method in structures resembling healthy and diseased lung tissue. The simulation results compare well to in vivo experiments and the analytical "cylinder" theory reported by Yablonskiy et al.

We report the use of a boundary wrapping method to create infinitely repeating structures. The technique is useful for reducing the number of elements required for a simulation, and hence allows a reduction in computation time. However, it is only applicable for structures that possess tessellating features. This was found to be useful for eliminating boundary effects in our simulations, however, it is debatable whether tessellating structures are valid for modeling lung tissue.

Diffusion within simulated porous structures yielded an ADC value that was virtually independent of b-value for the range of parameters studied. This was partly expected since the root-mean-squared distance traveled by the gas during the time 2δ was comparatively long compared to the pore sizes investigated. The results indicate that a continuous porous structure is not a suitable candidate for characterizing diffusion within healthy lung tissue, since the ADC is virtually independent of b-value for the gradient waveforms studied. A more suitable model may be a fractured porous media, where many of the pores would have blind endings. However, it can be argued that such a model is analogous to the "tree-like" and "grape-like" models studied here.

Two-dimensional simulations were conducted on "grape-like" and "tree-like" models. The structures were created using dimensions applicable to lung physiology, i.e., branch lengths and airway diameters had length scales ranging from ≈0.1 to 3 mm. The aims were, firstly, to provide a model for comparing simulation results to actual in vivo measurements, and secondly, to probe the robustness of the "cylinder" model. However, we made a significant approximation to make the results applicable to diffusion in 3D. Despite this, the result did agree with the diffusion measurements in vivo, and data fitted relatively well to the "cylinder" model. However, significant mismatch was found between the actual diameters of the airways and the diameters obtained from fitting. Also, in the simulations emulating emphysema the data deviated strongly from the "cylinder" theory, which is also highlighted in [11].

We found that results from simulations and in vivo measurements agree with the results of Yablonskiy et al.—that is diffusion is anisotropic and is mainly characterized by two diffusion components, D_L and D_T. However, the results from simulations (not all are shown), do not follow theory exactly, and suggest that other factors such as branch inter-connectivity and perhaps tortuosity must be taken into account. Also, applying the "cylinder" model for healthy lung tissue yields plausible results, however, the model breaks down where there has been significant lung destruction.

As previously reported by Yablonskiy et al. [11] and Maier et al. [9] the ADC in healthy lung tissue varies as a function b-value. Our simulation results and in vivo experiments agree with these findings, and suggests that future studies of the ADC in healthy and diseased lungs should attempt to take this into account.

Acknowledgments

The European Commission, Framework V, Polarised Helium to Image the Lungs (PHIL) Project for support.

Amersham Health (Durham NC) for polarising equipment.

References

[1] H.U. Kauczor, X.J. Chen, E.J.R. van Beek, W. Schreiber, Pulmonary ventilation imaged by MRI: at the doorstep of clinical application, Eur. Respir. J. 17 (2001) 1–16.

[2] H.E. Moller, X.J. Chen, B. Saam, K.D. Hagspiel, G.A. Johnson, T.A. Altes, E.E. De Lange, H.U. Kauczor, MRI of the lungs using hyperpolarized noble gases, Magn. Reson. Med. 47 (2002) 1029–1051.

[3] E.O. Stejskal, J.E. Tanner, Spin diffusion measurements: spin echoes in the presence of a time-dependent field gradient, J. Chem. Phys. 42 (1965) 288–292.

[4] J.P. Mugler III, J.R. Brookeman, J.Knight-Scott, T. Maier, E.E. de Lange, P.L. Bogorad, Regional measurement of the ^{3}He diffusion coefficient in the human lung, in: Proceedings of the 6th Meeting of ISMRM, Sydney, 1998.

[5] B.T. Saam, D.A. Yablonskiy, V.D. Kodibagkar, J.C. Leawoods, D.S. Gierada, J.D. Cooper, S.S. Lefrak, M.S. Conradi, MR imaging of diffusion of ^{3}He gas in healthy and diseased lungs, Magn. Reson. Med. 44 (2000) 174–179.

[6] M. Salerno, E.E. de Lange, T.A. Altes, J.D. Truwit, J.R. Brookeman, J.P. Mugler III, Emphysema: hyperpolarized helium 3 diffusion MR imaging of the lungs compared with spirometric indexes-initial experience, Radiology 222 (2002) 252–260.

[7] A.J. Swift, S. Fichele, N. Woodhouse, M.N.J Paley, E.J.R. van Beek, J.M. Wild, Anterior to posterior variations of the ADC of inhaled ^{3}He in healthy lungs, in: International Society for Magnetic Resonance in Medicine (ISMRM), Toronto, 2003, pp. 1402.

[8] J.C. Liner, S. Weissman, Determination of the temperature dependence of gaseous diffusion coefficients using gas chromatographic apparatus, J. Chem. Phys. 56 (1972) 2288–2290.

[9] T. Maier, J. Knight-Scott, V.M. Mai, J.P. Mugler III, J.R. Brookeman, Restricted diffusion of hyperpolarized ^{3}He in the human lung, in: International Society for Magnetic Resonance in Medicine (ISMRM), Sydney, 1998, pp. 1913.

[10] M. Salerno, J.R. Brookeman, J.P. Mugler III, Time-dependent hyperpolarized ^{3}He diffusion MR imaging: initial experience in healthy and emphysematous lungs. in: International Society for Magnetic Resonance in Medicine (ISMRM), Glasgow, 2001, pp. 950.

[11] D.A. Yablonskiy, A.L. Sukstanskii, J.C. Leawoods, D.S. Gierada, G.L. Bretthorst, S.S. Lefrak, J.D. Cooper, M.S. Conradi, Quantitative in vivo assessment of lung microstructure at the alveolar level with hyperpolarized ^{3}He diffusion MRI, Proc. Natl. Acad. Sci. USA 99 (2002) 3111–3116.

[12] H. Hagslatt, B. Jonsson, M. Nyden, O. Soderman, Predictions of pulsed field gradient NMR echo-decays for molecules diffusing in various restrictive geometries. Simulations of diffusion propagators based on a finite element method, J. Magn. Res. 161 (2003) 138–147.

[13] C.L. Chin, F.W. Wehrli, S.N. Hwang, M. Takahashi, D.B. Hackney, Biexponential diffusion attenuation in the rat spinal cord: computer simulations based on anatomic images of axonal architecture, Magn. Res. Med. 47 (2002) 455–460.

[14] M.H. Blees, The effect of finite duration of gradient pulses on the pulse-field–gradient NMR method for studying restricted diffusion, J. Magn. Res. A 109 (1994) 203–209.

[15] P. Callaghan, Principles of Nuclear Magnetic Resonance Microscopy, Oxford University Press, Oxford, 1991.

[16] L.Z. Wang, A. Caprihan, E. Fukushima, The narrow-pulse criterion for pulsed-gradient spin-echo diffusion measurements, J. Magn. Res. 117 (1995) 209–219.

[17] C.H. Neuman, Spin echo of spins diffusing in a bounded medium, J. Chem. Phys. 60 (1974) 4508–4511.

[18] G.P. Zientara, J.H. Freed, Spin-echoes for diffusion in bounded, heterogeneous media: a numerical study, J. Chem. Phys. 72 (1980) 1285.

[19] J. Crank, The Mathematics of Diffusion, second ed., Oxford University Press, London, 1975.

[20] J.B. West, Pulmonary Pathophysiology, Williams & Wilkins, London, 1998.

[21] A.B. Lumb, Applied Respiratory Physiology, Butterworth–Heinemann, Oxford, 2000.

[22] R.W. Mair, P.N. Sen, M.D. Hürlimann, S. Patz, D.G. Cory, R.L. Walsworth, The narrow pulse approximation and long length scale determination in xenon gas diffusion NMR studies of model porous media, J. Magn. Reson. 156 (2002) 202–212.

[23] R.W. Mair, G.P. Wong, D. Hoffmann, M.D. Hürlimann, S. Patz, L.M. Schwartz, R.L. Walsworth, Probing porous media with gas diffusion NMR, Phys. Rev. Lett. 83 (1999) 3324–3327.

[24] P.P. Mitra, P.N. Sen, L.M. Schwartz, Short-time behavior of the diffusion coefficient as a geometrical probe of porous media, Phys. Rev. B 47 (1993) 8565–8574.

[25] C. Kittel, Introduction to Solid State Physics, Wiley, New York, 1966.

[26] W.G. Schreiber, A. Bink, K. Gast, K. Katsaros, J. Schmiedeskamp, E. Mayer, A. Vogel, N. Weiler, H.U. Kauczor, Diffusion-weighted MRI of the lung using hyperpolarized helium-3, in: Helion 02, Oppenheim, Germany, 2002, p. 36.